Excitations in high-dimensional random-field Ising magnets

Björn Ahrens and Alexander K. Hartmann*
Institute of Physics, University of Oldenburg, 26111 Oldenburg, Germany
(Received 2 January 2012; revised manuscript received 3 May 2012; published 20 June 2012)

Domain walls and droplet-like excitation of the random-field Ising magnet are studied in $d = \{3,4,5,6,7\}$ dimensions by means of exact numerical ground-state calculations. They are obtained using the established mapping to the graph-theoretical maximum-flow problem. This allows us to study large system sizes of more than 5×10^6 spins in exact thermal equilibrium. All simulations are carried out at the critical point for the strength h of the random fields, $h = h_c(d)$. Using finite-size scaling, energetic and geometric properties like stiffness exponents and fractal dimensions are calculated. Using these results, we test (hyper)scaling relations, which seem to be fulfilled below the upper critical dimension $d_u = 6$. Also, for $d < d_u$, the stiffness exponent can be obtained from the scaling of the ground-state energy.

DOI: 10.1103/PhysRevB.85.224421 PACS number(s): 75.10.Nr, 75.40.−s, 75.50.Lk, 64.60.De

I. INTRODUCTION

The random-field Ising magnet (RFIM) is one of the most frequently studied models for magnetic systems with quenched disorder. For $d = 3$ and higher dimensions,[1] it is known to undergo a phase transition[2–13] at a critical temperature T_c which depends on the disorder strength. For low temperatures and weak disorder the ferromagnetic interactions dominate, and the system is ferromagnetically long-range ordered. For large temperature or strong disorder, the RFIM exhibits no long-range order and behaves like a paramagnet in a field.

Numerically, the nature of this phase transition can be studied in many cases conveniently by means of exact ground-state (GS) calculations (see below), based on an established mapping to the graph-theoretical maximum-flow problem. This allows us to treat large system sizes in thermal equilibrium, in contrast to Monte Carlo simulations. For Gaussian disorder, the phase transition is of second order along the full transition line and can be characterized by critical exponents in the usual way, like ν, describing the divergence of the correlation length, and α, describing the behavior of the specific heat. Nevertheless, the RFIM behaves differently compared to the standard ferromagnet. In particular, the hyperscaling relation $d\nu = 2 - \alpha$ has to be changed[14] by including a positive parameter θ, yielding

$$\nu(d - \theta) = 2 - \alpha\,. \tag{1}$$

In general, the value of θ can be obtained directly from the scaling of domain-wall energies, e.g., induced by changing the boundary conditions, and is known as the *stiffness exponent*. The study of such domain-wall excitations was pioneered in the field of spin glasses.[15,16] Here, a comprehensive understanding of the nature of the behavior of two-dimensional spin glasses could be obtained,[17,18] which turned out to be compatible with the droplet picture.[15,19–21]

According to the droplet picture, the energy scaling of droplet-like excitations should be the same as for domain walls. For two-dimensional spin glasses, this was recently confirmed via using modified GS algorithms.[22–24] Later on, the value of θ was also determined in higher dimensions[25–29] up to the upper critical dimension, in this case via (heuristic) ground-state calculations before and after changing the boundary conditions.

For the RFIM, which is the subject of this work, domain-wall studies similar to the spin-glass case, i.e., based on GS calculations, were performed for three and four dimensions,[7,11] but to our knowledge not in higher dimensions. Droplet-type low- or lowest-energy excitations have only been obtained in three dimensions so far.[12,30] For three dimensions at finite temperature, also free-energy barriers were calculated recently.[31,32]

Furthermore, the prediction for the RFIM upper critical dimension $d_u = 6$ was confirmed[13] via exhaustive exact GS calculation up to $d = 7$. This shows that the RFIM can be investigated conveniently by numerical exact algorithms even close to and above the upper critical dimension.

Hence, it is the purpose of this work to study domain-wall and droplet excitations of the RFIM in dimensions $d = 5,6,7$ (and for $d = 3,4$ for comparison), similar to the corresponding $d = 2$ studies for spin glasses, with the striking difference that for the RFIM an exact polynomial-time GS algorithm is available for any dimension, allowing us to treat much larger system sizes of more than 5×10^6 spins in thermal equilibrium. Another difference is that we performed the study for the RFIM right at the zero-temperature disorder critical point (like the previous work in lower dimensions) since the scaling in the ferromagnetic and paramagnetic phases should be trivial. We analyzed energetic and geometric properties of the excitations using finite-size scaling. We compare the results of different excitations, which should agree according to the droplet picture, and verify the above-mentioned hyperscaling relation. Also we compare the geometric (fractal) properties of these excitations. Treating system sizes up to and above the upper critical dimension allows us to observe the transition to mean-field behavior.

To state the model in detail, the RFIM consists of N Ising spins $S_i = \pm 1$ located on the sites of a hypercubic lattice with periodic boundary conditions (PBC) in all directions. The spins couple to each other and to local net fields. Its Hamiltonian reads

$$\mathcal{H} = -J \sum_{\langle i,j \rangle} S_i S_j - \sum_i (h\varepsilon_i)\, S_i\,. \tag{2}$$

It has two contributions. The first covers the spin-spin interaction, where J is the ferromagnetic coupling constant

between two adjacent spins and $\langle i,j\rangle$ denotes pairs of next-neighbor spins. The second part of the Hamiltonian describes the coupling to local fields $h_i = h\varepsilon_i$. The factor h is the disorder strength, and ε_i the quenched disorder, i.e., Gaussian distributed with zero mean and unit width.

This paper is organized as follows: In Sec. II we describe in principle how the GSs are calculated. The following section covers the definition and use of the different excitations and their theoretical background. Then we state our results in Sec. IV and finish with our conclusions and discussion.

II. GROUND STATES

The phase space of the RFIM consists of a ferromagnetic phase and a paramagnetic phase. The transition from one phase to the other takes place at a critical point $P_c = (h_c, T_c)$. The transition can be triggered by varying the temperature T or varying the standard deviation h of the disorder distribution. From Ref. 33, it is known via renormalization group calculations that the critical behavior of the RFIM is controlled from the zero-temperature fixed point. Hence, it is possible to focus on $T = 0 = \text{const}$ and vary h to study the phase transition. Here, we concentrated on $T = 0, h \approx h_c$, to study excitations right at at the critical point.

At $T = 0$ it is possible to calculate exact ground states in a very efficient way. Following an approach from Refs. 34 and 35, a d-dimensional hypercubic realization of the disorder $\{h\varepsilon_i\}$ can be mapped to a graph with $N + 2$ nodes and $(d + 2)N + 1$ edges with suitable edge capacities, where N is the number of spins of the RFIM. On this graph a sophisticated maximum-flow/minimum-cut algorithm can be applied.[36,37] The resulting minimum cut directly corresponds to the GS spin configuration $\{S_i\}$ of that specific realization of the disorder. For our simulations the implementation of the maximum flow algorithm from the LEDA library[38] is used. For the RFIM, the actual runtime of the algorithm increases only slightly stronger than linear with the number N of spins.[39]

III. DOMAIN WALLS AND DROPLET EXCITATIONS

We studied two types of excitations, domain walls and droplets. The domain walls treated in this work separate spin regions which are affected by changed (boundary) conditions from unaffected spins. Following Ref. 7 we forced boundary spins along distinct directions, i.e., up (+) or down (−), at opposite boundaries. Hence, the PBC are released in that direction, while they are preserved in the remaining $d - 1$ directions. We calculated the GSs for the four possible combinations, $+-$, $-+$, $++$, and $--$. Three types of spin regions can be distinguished. The first type can be flipped, changing a single boundary condition, e.g., from $++$ to $+-$. We call these spin regions *strong controllable*. The second type is just called *controllable* if it can be flipped by changing both boundary conditions. The third type forms fixed, stable *islands*, unaffected by any boundary-condition change. Examples for regions of such spins are shown in Fig. 1.

We also compare two kinds of droplet excitations of the GS. In both cases, first a GS $\{S_i^{(0)}\}$ is calculated for full PBC of each realization.

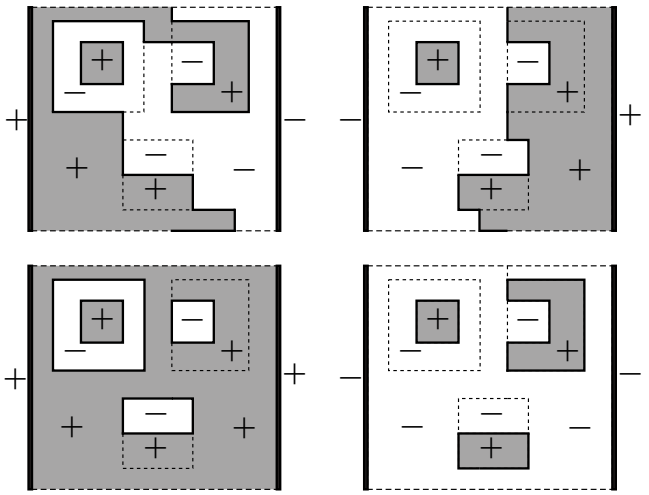

FIG. 1. Fixing the boundary spins (black bars on the left and right of every sketch) forces controllable spins to the direction of the boundary sign. Areas with $s_i = +1$ are shaded gray, and areas with spins $s_i = -1$ are white. The $(d-1)$-dimensional surface between spins of opposite direction is called the domain wall (black lines). In some regions, the random fields may freeze the spins into boundary-independent stable islands. Islands may include opposite-directed islands. Hence, islands may also interfere with the domain wall. The dashed lines signal the border of islands within an area of equally oriented spins and, at the top and the bottom, the periodic boundary conditions in the remaining $d - 1$ directions.

(i) The first type of excitation is obtained by now fixing $(L/3)^d$ spins in the center opposite their ground-state orientation. This is inspired by the approach of Ref. 40 for a disordered solid-on-solid model. This effect can be achieved conveniently by applying strong local fields $\tilde{h}_i$ in the desired direction for the fixed spins. Also, we fixed the spins on the hyperplanes of the boundary in parallel to the GS orientation.[20] Hence, now the local fields read

$$h\epsilon_i' = \begin{cases} -h_{\text{big}} S_i^{(0)} & i \in \text{center}, \\ h_{\text{big}} S_i^{(0)} & i \in \text{boundary}, \\ h\epsilon_i & \text{otherwise}, \end{cases} \tag{3}$$

where h_{big} is large enough that it fixes the GS orientation, e.g., $h_{\text{big}} = J(2d + 1)$. Note that the spins inside the center area create a contribution to the droplet energy via the local fields. To exclude this unwanted effect, we set the local fields ε in the center region to zero already for the first GS calculation of $\{S_i^{(0)}\}$. Via a recalculation of the GS of the modified system $(\{S_i'\})$, i.e., for the fields $h\epsilon_i'$, this leads to a large excitation with respect to the first GS $\{S_i^{(0)}\}$. Note that the excitation does not include the boundary; i.e., it is impossible that the full system flips over. Below, we refer to these excitations as *bulk-induced droplets*; see Fig. 2. From the definition it is clear that these excitations involve $O(L^3)$ spins. Therefore, they come very close to the definition of droplets in droplet theory.[20,21] To our knowledge, such droplets have not been studied for the RFIM.

(ii) The other type of excitation, called *single-spin-induced droplets*, consists of flipping only the very center spin and freezing it antiparallel to its ground-state orientation, again including fixing boundary spins in parallel to the GS. In the

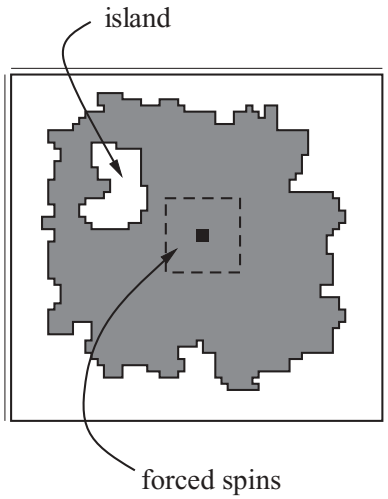

FIG. 2. Spinwise difference of the pure GS and a droplet. Unchanged spins are shown as white areas ($S_i^{(0)} - S_i' = 0$), and changed spins are displayed in gray ($|S_i^{(0)} - S_i'| = 2$). The excitation is generated, freezing the spins on the boundaries to their pure GS orientation, while the spins in a region in the center are frozen inverted to their ground-state orientation (a black dot for the single-spin-induced droplets and a dashed square for the bulk-induced droplets). Under these frozen-spin constraints a new GS is calculated. This new configuration is an excitation with respect to the original GS. The resulting droplet may spread to an arbitrary shape with a fractal surface. It also may contain islands.

same way as for the bulk-induced droplets, this is achieved by applying strong local fields:

$$h\epsilon_i' = \begin{cases} -h_{\text{big}} S_i^{(0)} & i = \text{center spin}, \\ h_{\text{big}} S_i^{(0)} & i \in \text{boundary}, \\ h\epsilon_i & \text{otherwise}. \end{cases} \tag{4}$$

The droplet created in such a way will include the center spin, but not the boundary. Theses single-spin-induced droplets will be usually smaller than the bulk-induced droplets. Such excitations have been studied in $d = 3$ so far.[30]

Hence, for each realization $\{h\varepsilon_i\}$ of the disorder, we obtained seven different (ground-state) configurations for different types of boundary conditions/constraints [PBC, $(++)$, $(--)$, $(+-)$, $(-+)$, bulk-induced droplets, and single-spin-induced droplets]. Technically, to obtain the droplets, we extracted the absolute differences between the spin configuration of two or more GSs via linear combinations of the configurations. Spins with the same properties add to the same value and form connected clusters. These clusters were obtained using a breadth-first-search algorithm. In this way, the calculation of geometric properties of the clusters was very convenient. For the droplets, we measured the domain wall enclosing the droplet, i.e., the droplet surface. In the case of different boundary conditions, we are interested in different definitions of the domain walls, i.e., separating uncontrollable spins vs controllable spins and strongly controllable spins vs controllable spins and islands, allowing us to measure different related fractal exponents.

The surfaces are usually not flat or smooth; instead, a type of disorder-averaged surface $A_\circ$ exhibits asymptotically a fractal scaling behavior of the form

$$A_\circ = c_\circ L^{d_\circ}, \tag{5}$$

where $d_\circ$ is the corresponding fractal dimension and $c_\circ$ is a constant. Depending on the different boundary and droplet conditions, several fractal exponents can be deduced. Partially following the definitions of Ref. 7, we measured the following.

d_s is the surface exponent describing the dimensionality of the (hyper)surface of unchanged spins within two GSs of $++$ and $+-$ boundary conditions. Technically, we calculate $x_i = |s_i^{++} - s_i^{+-}| = \{0,2\}$ and count the bonds between the difference-zero cluster (unchanged spins) and difference-two cluster (changed spins).

d_I is the incongruent interface exponent describing the dimensionality of the surface of unchanged spins within the three GSs of $++$, $+-$, and $--$ boundary conditions. This domain wall does not include any parts of stable islands. In detail, we calculate $x_i = s_i^{--} + s_i^{++} - 2s_i^{-+} + 4 = \{2,4,6\}$. x_i results in 2 if s_i is strongly controllable. Spins with $x_i = 4$ belong to a stable island and $x_i = 6$ if s_i is just controllable. For the incongruent boundary only the bonds between the difference-two cluster and difference-six cluster are counted.

d_J is the exchange stiffness exponent, describing the scaling behavior of the sum of signed bonds, positive in the $+-$ and $-+$ configurations and negative for the $++$ and $--$ configurations.

d_{B} is the fractal exponent of the surface between all flipped and unflipped spins, i.e., the number of bonds between these, for bulk-induced droplets, including islands.

$d_{\text{B}}^{(o)}$ is the same as d_{B}, but excluding islands.

d_1 is the fractal exponent of the surface between all flipped and unflipped spins, induced by single-spin-induced excitations, including islands.

$d_1^{(o)}$ the same as d_1, but excluding islands.

In the case of droplet excitations, we measured additionally the disorder-averaged volume V, i.e., the average number of spins in the cluster of droplet spins.

In addition to the geometric properties of domain walls and droplets we are interested in the stiffness exponent θ, and we compare three different types of excitations. The first approach is based on the symmetrized stiffness Σ defined by Middleton and Fisher,[7] i.e., the disorder-averaged symmetrized sum of the boundary-condition-dependent energies.

$$\Sigma \equiv \langle E_{+-} + E_{-+} - E_{++} - E_{--} \rangle / 2\,, \tag{6}$$

where E_{pq} is the GS energy for boundary condition $pq \in \{++, --, +-, -+\}$ and $\langle\cdot\rangle$ denotes the disorder average.

A detailed picture of the resulting configurations can be found in Fig. 1. Close to criticality, the average stiffness can be assumed to scale as[7]

$$\Sigma(L) \sim L^{\theta}\,, \tag{7}$$

where θ denotes the stiffness exponent. According to droplet theory, the energy for other types of excitations of the order of system sizes should scale with the same exponent. Hence, for the bulk-induced droplets, one should be able to observe

$$\Delta E_{\text{B}}(L) \sim L^{\theta}\,, \tag{8}$$

where ΔE_{B} is the average of the excitation energy of the droplet, i.e., the energy of the droplet configuration for the

original value of the fields minus the GS energy for the same original values of the fields.

Note that the single-spin-induced droplets tend to be small; i.e., they are not of the order of the system size. Hence, one cannot directly measure θ from the scaling of the droplet energy. Instead, for the third approach, we follow the arguments of Ref. 30. Therein, it is shown that the distribution of single-spin-induced droplet radii scales as $p(R) \sim R^{-\theta}$.

IV. RESULTS

We performed exact ground-state calculations for

$$d = 3 : L = 8 \cdots 128 \text{ with } 11 \times 10^4 \cdots 1 \times 10^5,$$
$$d = 4 : L = 6 \cdots 45 \text{ with } 2 \times 10^4 \cdots 2 \times 10^5,$$
$$d = 5 : L = 6 \cdots 20 \text{ with } 2 \times 10^3 \cdots 1 \times 10^4,$$
$$d = 6 : L = 6 \cdots 14 \text{ with } 55 \cdots 1 \times 10^4,$$
$$d = 7 : L = 4 \cdots 8 \text{with } 1 \times 10^3 \cdots 1 \times 10^4,$$

where the range of numbers indicates the number of realizations of the disorder and the largest size exhibits the smallest number of realizations. Note that for $d = 4$, we studied $L = 45$ only for the bulk-induced droplets, whereas we did not included results for bulk-induced droplets in $d > 5$. In general, due to computer main memory restrictions we are limited to system sizes below 5×10^6 spins. We start our analysis with the geometric properties of the domain walls.

A. Domain walls

The surfaces of the three different defined boundary-induced domain walls scale with plain and very clear power laws. For example, the scaling of the simple domain wall, i.e., $(++)/(+-)$ (yielding the fractal exponent d_s), is shown in Fig. 3. Error bars[41] were obtained as standard error bars from the empirical variance. The other plots look quite the same with the same precision. The scaling exponents d_s, d_J, and d_I were found with high *statistical* accuracy. They are stated in Table I. Note that the upper limit for any fractal dimension is d; hence the result for d_s at $d = 7$ is an artifact created by the small range of sizes which is accessible at this high dimension. Also, the obtained exponents depend on the fit range, reflecting possible systematic correction to the limiting scaling behavior of Eq. (5). To estimate such systematic errors, we have performed fits for different ranges, leading to the final results which are displayed in Table II. Given this accuracy, the results for d_J may d_I agree or differ, particularly in large dimensions (see discussion in Sec. V), but d_s differs, comparable to the previously obtained results[7,11] for $d = 3,4$.

TABLE I. Fit parameters for the scaling of the different surface definitions, i.e., pure surface, Σ_J, and the incongruent parts of the domain walls.

d	c_s	d_s	c_J	d_J	c_I	d_I
3	0.90(3)	2.367(9)	5.9(2)	2.178(8)	0.96(3)	2.28(1)
4	0.674(8)	3.924(3)	9.0(2)	3.001(7)	1.261(6)	3.231(2)
5	0.98(2)	4.96(1)	11.7(1)	3.800(4)	1.97(1)	3.925(3)
6	1.37(9)	5.88(3)	16.2(8)	4.56(2)	3.5(2)	4.51(3)
7	1.11(9)	7.06(7)	15(1)	5.57(4)	3.3(3)	5.49(5)

We continue by calculating the stiffness exponents. First, the well-established ansatz according to Eq. (6) is used for $d = 3,4,5,6,7$. Our data show well-behaved power laws in each dimension; see Fig. 4. The fits of the data points follow Eq. (7), and the parameters are stated in Table III, where the resulting estimate for the stiffness exponent θ is denoted θ_{dw}. Varying the ranges of fitted sizes leads to the final estimates, again stated in Table II.

B. Droplets

Concerning the droplet behavior, we start with the fractal surface properties of the droplets. We start by using a scatter-plot to obtain the relation between the surface and volume of single-spin-induced droplets. Theoretically, it should follow a power law of the form

$$A \sim V^{d_1/d}. \tag{9}$$

The fractal surface exponents with and without stable islands can be obtained this way, depending on whether the islands are included in the calculation of A. Indeed, the results exhibit

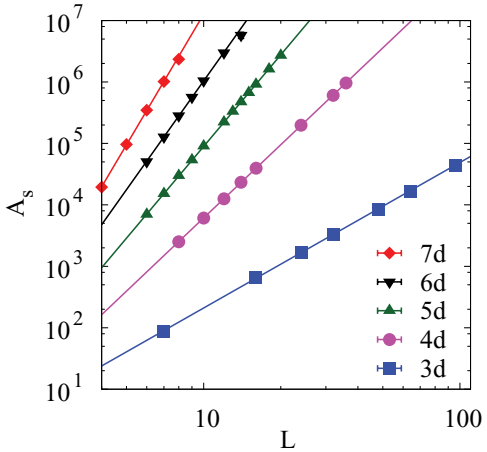

FIG. 3. (Color online) Simple surface of domain walls. Most error bars are smaller than the symbol size. The lines show power-law fits according to Eq. (5).

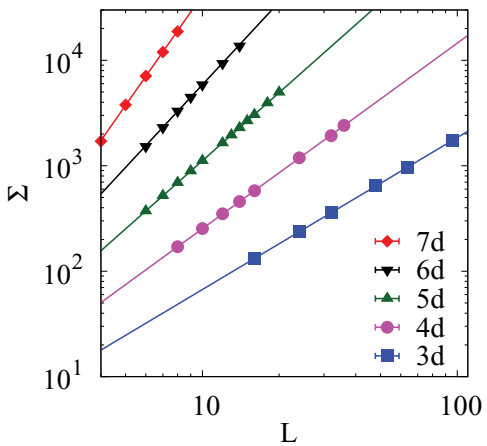

FIG. 4. (Color online) Stiffness, as defined in Eq. (6). Most error bars are smaller than the symbol size. Lines display results of fits to power-laws according to Eq. (7).

TABLE II. Previous results[7,11,13] compared to our final results. The first part of the final results contains different estimates for the stiffness exponent, while the second part contains measurements for the fractal properties of domain walls. Note that the values stated here differ usually from the values given in the lists of fit parameters since the former include systematical errors, which were estimated by varying the range of fitted system sizes and observing the change of the resulting parameters.

	$d=3$	$d=4$	$d=5$	$d=6$	$d=7$
Previous results					
h_c	2.28(1)	4.18(1)	6.02(2)	7.78(1)	9.48(3)
β	0.017(5)	0.13(5)	0.25(1)	0.50(5)	0.50(5)
γ	1.98(7)	1.57(10)	1.3(1)	1.07(5)	1.0(2)
α	0	0	0	0	0
ν	1.37(9)	0.78(10)	0.60(3)	0.50(5)	0.47(5)
$\tilde{\theta}=\gamma/\nu$	1.4(2)	2.0(4)	2.3(3)	2.1(5)	2.2(5)
Final results					
θ_{E}	1.49(3)	1.81(6)	2.03(2)	2.42(2)	2.42(2)
θ_{dw}	1.44(2)	1.75(2)	2.15(1)	2.60(2)	3.5(1)
d_J-1/ν	1.4(1)	1.65(15)	2.1(1)	2.5(2)	3.5(1)
θ_{B}	1.51(2)	1.8(1)			
d_s	2.37(2)	3.92(6)	4.9(2)	5.8(8)	6.9(2)
d_1	2.32(1)	3.73(10)	4.9(1)	5.9(1)	6.9(1)
d_B	2.35(2)	3.79(4)	4.6(1)		
d_J	2.14(3)	2.93(2)	3.79(2)	4.54(2)	5.5(1)
d_I	2.25(2)	3.23(1)	3.92(1)	4.5(2)	5.4(2)

clear power laws; see Fig. 5. Additionally, for each dimension the data points for other system sizes L scatter around the same line. The fit parameters are listed in Table IV for fixed system sizes. The fractal exponents with and without enclosed islands do not differ significantly. We have observed slight changes in the value of d_1 when varying the system size L (unless using very small system sizes where the fitted value of d_1 is much smaller). Hence, the final values we quote (c.f. Table II) are slightly different and involve larger error bars than the pure statistical error bars. When approaching large dimensions d_s gets close to the dimension of the system, particularly right at the upper critical dimension. The result for the fractal dimensions is, given the unknown correlations to scaling, in fair agreement with the results for d_s, as shown in Table I.

The bulk-induced droplets have the disadvantage that a smaller effective range of sizes if accessible: The minimal system size to generate such a droplet excitation must be $L=6$. In the linear direction, one spin is used to fix the boundary and at least one other is needed at the very center to form the "large core." Therefore, only two spins in each direction are left to form the droplet. In the same way, also for larger sizes, the volume available for the droplets to form is smaller, leading to stronger finite-size corrections; see below. This means, for $d>5$, that the range of system sizes ($L\geqslant 6$) is too small to observe the leading scaling behavior. Hence, we restrict our analysis of the bulk-induced droplets to $d=3,4$ and $d=5$.

TABLE III. Fit parameters for θ according to Eq. (7).

d	a	θ_{dw}
3	2.42(1)	1.442(2)
4	4.40(3)	1.760(3)
5	7.97(5)	2.146(3)
6	14.6(5)	2.60(1)
7	14.3(6)	3.45(2)

In Fig. 6 a scatterplot of the enclosing surface as a function of the volume can be seen. For the fits the ansatz according to Eq. (9) was made, but using d_B instead of d_1. The fit parameters can be obtained from the large number of data points by using the data points for all system sizes in one fit, with high statistical accuracy. The fit parameters can be found in Table V. Given the small ranges of system sizes here and unknown corrections to scaling, the agreement with the results for the single-spin-induced droplets is fair.

Systematic finite-size corrections are neglected by this single fit of the scatterplot data. Hence, to estimate these corrections, leading to the results stated in Table II, we proceeded as follows: Instead of observing the scatterplot, the

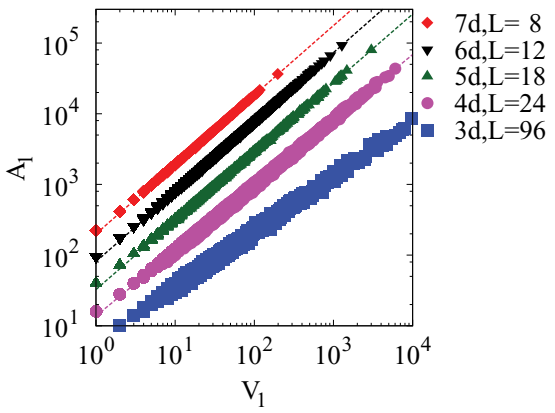

FIG. 5. (Color online) Scatterplot of the enclosing surface, i.e., not counting islands inside the droplet, of single-spin-induced droplets as function of their volume. The surface is scaled with a factor of $k=1,2,4,8,16$ for $d=3,4,5,6,7$ to separate the data visually.

TABLE IV. Fit parameters for the scaling of the enclosing surface and ragged surface for single-spin-induced droplets, calculated for a large system size with a high sample number, with system sizes as in Fig. 5.

d	c_1	d_1	$c_1^{(o)}$	$d_1^{(o)}$
3	6.07(2)	2.32(1)	6.02(2)	2.33(1)
4	6.88(1)	3.70(1)	6.87(1)	3.70(1)
5	8.15(3)	4.87(1)	8.51(2)	4.87(1)
6	10.13(1)	5.91(1)	10.13(1)	5.91(1)
7	12.49(3)	6.88(1)	12.53(3)	6.86(1)

mean of the enclosing surface can be analyzed as a function of the system size. A power law $A_B(L) = c_B(L - L_0)^{d_B}$ leads to the best fits. The length-scale correction L_0 covers finite-size effects. Of course, an ansatz using a correction term $c_B L^{d_B}(1 + c_2 L^{d'})$ can be used too, but the correction term involves one more parameter. Anyway, fitting $A_B(L)$ leads to similar exponents compared to those obtained from the scatterplot; see Table VI. Again, the results for the different approaches for surface measurement do not lead to significantly different results.

Next, we discuss the energetic properties of droplets to estimate the stiffness exponent θ. The singe-spin droplets are known to be very small.[30] This property prohibits the direct measurement of the stiffness exponents from the relation of droplet energy to linear droplet size. Nevertheless, the distribution of droplet radii R follows[30] approximately a power law $P(R) \sim R^{-\theta}$ when the data are binned logarithmically. Hence, we obtained the distribution of droplet radii. For $d = 3,4,5$ a logarithmic binning of the data points is possible. For larger dimensions, the achievable system sizes seem to be too small to get a histogram of sufficient statistical quality. The histograms can be seen in Fig. 7. There exist regions in which the radii distribution follows $R^{-\theta}$ when using the values for θ_{dw} obtained from the domain-wall measurements. This confirms the results of Ref. 30 for higher dimensions, $d = 4,5$. Nevertheless, the distribution itself is not sufficient

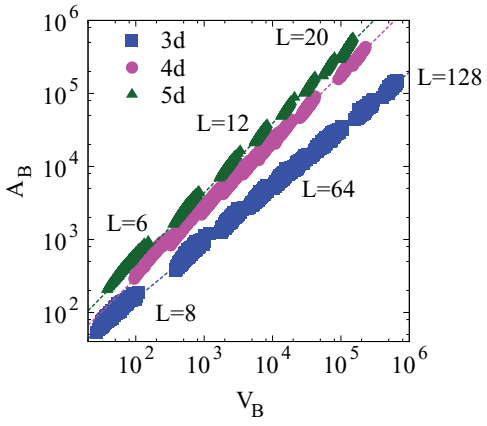

FIG. 6. (Color online) Scatterplot of the enclosing surface of bulk-induced droplets as a function of their volume for $d = 3,4,5$. The bottom right labels show system sizes of the $3d$ data, and the top left labels show those for $5d$; $4d$ is unlabeled.

TABLE V. Fit parameters for scaling the enclosing surface and ragged surface for bulk-induced droplets. For $d > 4$, high-quality data are not available for large-enough system sizes.

d	c_B	d_B	$c_B^{(o)}$	$d_B^{(o)}$
3	4.300(4)	2.3282(2)	2.761(3)	2.660(2)
4	4.085(3)	3.7257(2)	4.024(3)	3.7328(2)
5	6.10(3)	4.758(2)	6.10(3)	4.758(2)

to determine the stiffness in a meaningful way if the values of θ were not known from other sources.

For the bulk-induced droplets, their length scale is fixed to be $O(L)$, as assumed in droplet theory.[20,21] Hence, one could hope that the scaling of the droplet energy is governed by the (stiffness) exponent θ. We looked at the scaling of the difference between the GS energies of the original system and the GS for the bulk-induced droplets (calculated with the original set of random fields). The resulting average bulk droplet energies ΔE_{B} are shown in Fig. 8 for $d = 3,4$. A clear curvature is visible; hence there are strong finite-size corrections to Eq. (8). This can be explained by the fact that, due to the extensive size of the center area, the effective volume which is accessible for the droplet to arrange is much smaller. In particular this means that for the higher dimension $d > 4$ the linear sizes L which are accessible are too small to come even just near the final scaling behavior. Hence, we have restricted ourselves for the energetic properties of the bulk-induced droplets to dimensions $d = 3$ and 4. To include corrections to scaling, we fitted the data by using

$$\Delta E_B = a(L - L_0)^{\theta_{\mathrm{B}}}; \tag{10}$$

see Table VII. This fit approximately and heuristically describes the situation where the data are compatible with a power law only beyond a system size $L \geqslant L_0$, and it has already been used in finite-size data analysis in the past (see, e.g., Refs. 42 and 43). The minimum system size L_{min} which was included in the fit was chosen such that the fitting quality (measured by the weighted sum of square residuals per degree of freedom, denoted as WSSER/NDF in GUNPLOT) was acceptable, i.e., around 1. To estimate systematic corrections, we also performed fits for larger values of L_{min}, leading to the final results for θ_{B} as stated in Table II. We also tried a more standard scaling form $\Delta E'_B = a' L^{\theta'_B}(1 + eL^{-f})$, which carries one additional parameter. Nevertheless, the quality of the fit was smaller compared to the scaling form (10). Also, the resulting values of $\theta'_B = 1.43(15)$ ($d = 3$) and $\theta'_B = 1.74(35)$ ($d = 4$), although compatible with the values obtained from fitting to (10), exhibit much less accuracy. Hence we decided

TABLE VI. Fit parameters for scaling the enclosing surface and ragged surface for bulk-induced droplets when scaling the surface as a function of system size. For $d = 6,7$, a large-enough range of system sizes is not available.

d	c_B	L_0	d_B	$c_B^{(o)}$	$L_0^{(o)}$	$d_B^{(o)}$
3	1.37(8)	2.2(1)	2.35(2)	1.02(6)	1.88(9)	2.44(1)
4	0.49(5)	1.50(9)	3.79(3)	0.48(5)	1.49(9)	3.80(3)
5	0.8(2)	2.0(1)	4.54(6)	0.8(2)	2.0(1)	4.54(6)

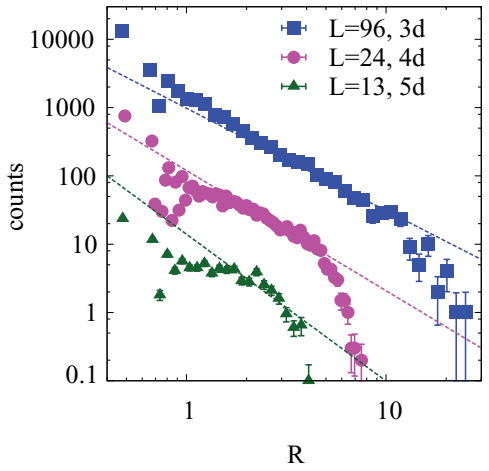

FIG. 7. (Color online) Number of single-spin-induced droplets with a radius in a specific interval for $d = 3$, $L = 96$; $d = 4$, $L = 24$; and $d = 4$, $L = 13$. The last two were down scaled by a factor 10 and 20, respectively. The lines are power laws using the stiffness exponents.

to finally state the results obtained from using the less common scaling form (10). Within error bars, these resulting values for the droplet stiffness are compatible with the results obtained for the domain walls. Hence, it appears that indeed the basic assumption of the droplet theory is true, that different types of excitations are universally described by the same exponents.

C. Scaling of ground-state energy

There seems to exist a third alternative way of determining the stiffness exponent, not related to externally induced domain walls and droplets. For spin glasses in finite and low dimensions with PBC, it has been conjectured[44] and numerically observed for two dimensions[45] that the finite-size behavior of the (total) GS energy E_L of the unperturbed system is given by

$$E_L = E_\infty + aL^\theta . \tag{11}$$

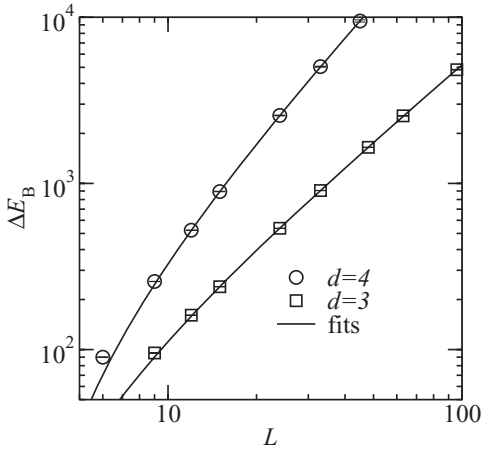

FIG. 8. Scaling of the excitation energy ΔE_B of bulk-induced droplets for $d = 3$ and $d = 4$. Lines show fits to power laws $\Delta E_B \sim (L - L_0)^\theta$, with $\theta = 1.50$ ($3d$) and $\theta = 1.91$ ($4d$).

TABLE VII. Fit parameters for scaling the droplet energy according to Eq. (10). The fits were performed for a range of system sizes ranging from $L_{\min}$ to the largest system sizes considered here.

d	$L_{\min}$	a	L_0	θ_B
3	15	5.34(15)	2.42(10)	1.501 (7)
4	12	7.41(18)	2.75 (5)	1.91 (1)

The explanation is that the PBC induce "hidden" domain walls (with respect to free boundary conditions) which dominate the finite-size corrections above higher-order contributions. Hence, we have reanalyzed the data of previous work.[6,10,13] The results of θ from fitting (11) to the GS energies can be found in Fig. 9; its exponents are given as θ_E in Table II. Compared with the results for the stiffness exponent θ_{dw}, the assumptions seem to be indeed true for $d < d_u = 6$ and maybe also at $d = d_u$ (given that we state here only statistical error bars, true error bars are likely larger). The assumption of Eq. (11) is certainly not true above the upper critical dimension. It seems rather that the exponent for the GS energy finite-size correction attains some mean-field value for $d \geqslant d_u$. Interestingly, θ_E agrees within the error bars with γ/ν in all dimensions $d = 3, \ldots, 7$.

V. CONCLUSION AND DISCUSSION

To calculate the ground states of the RFIM numerically, we applied a well-known mapping to the maximum-flow problem. Using efficient polynomial-time-running maximum-flow/minimum-cut algorithms, we were able to study large systems sizes up to 5×10^6 spins in exact equilibrium at $T = 0$.

Comparing the GS configurations obtained from different constraints leads to suitably defined domain-wall and droplet excitations. We obtained fractal surface exponents and the stiffness exponent in $d = 3,4,5,6,7$ for these excitations; see the final results in Table II. The values for domain walls stated in the literature[7,11] for $d = 3,4$ could be recovered. For all dimensions, different types of excitations are described, within the error bars, by the same value of the stiffness exponents, as assumed by droplet theory.[20,21] In particular,

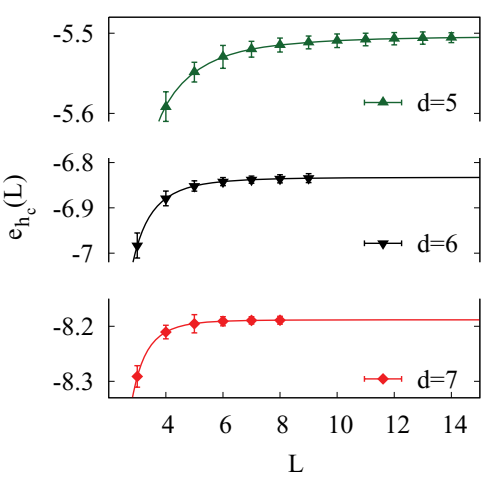

FIG. 9. (Color online) Scaling of the ground-state energy at the critical point. The lines show fits to Eq. (11).

(bulk-induced) droplet excitations have been calculated for the RFIM and have been found to be compatible with domain walls. Also, the result for θ_{dw} is compatible with the scaling relation $d_J - 1/\nu$, which is fulfilled within the error bars for all dimensions. Furthermore, the scaling inequality[46,47] $d/2 - \beta/\nu \leqslant \theta \leqslant \theta/2$ is fulfilled in all dimensions.

On the other hand, the hyperscaling relation (1) is fulfilled within error bars only for $d = 3,4,5$ but not for $d = 6,7$. Usually, hyperscaling relations involving the dimension d are not valid in the mean-field regime, i.e., above the upper critical dimension. Right at the upper critical dimension, where (1) predicts $\theta = 2$, logarithmic corrections become important;[48–50] hence one has presumably to reach large system sizes to observe the leading behavior. Here, by studying system sizes $L \leqslant 14$ we reach the limit of our numerical resources (meaning that we are able to obtain exact ground states for systems having more than 7×10^6 spins). Thus, it seems extremely impossible with current resources and known algorithms to verify whether the apparent failure of hyperscaling at $d = 6$ is only due to strong finite-size corrections.

Also, the fractal properties of the droplets and domain walls found for lower dimensions extend to larger dimensions. In particular, the "geometrically" measured values d_s, d_1, and d_{B} agree for all dimensions within the error bars. Finally, the values for d_I and d_J, measuring different fractal properties of the domain walls, are clearly different within the error bars from d_s, d_1, and d_{B}. Also, below the upper critical dimension $d_u = 6$, d_I and d_J are different from each other within the error bars, while the values are compatible with each other for $d \geqslant 6$. This seems to be another property of the mean-field limit, that certain properties which are different for $d < d_u$ agree for $d \geqslant d_u$.

ACKNOWLEDGMENTS

We thank K. Binder, S. Boettcher, A. Hucht, O. Melchert, M. Mézard, U. Nowak, H. Rieger, D. Sherrington, and D. Stauffer for useful discussions. The calculations were carried out on Großrechner Oldenburg für Explizit Multidisziplinäre Forschung (GOLEM) and the High-End Computing Resource Oldenburg (HERO) at the University of Oldenburg funded by the DFG (INST 184/108-1 FUGG) and by the Ministry of Science and Culture (MWK) of the state of Lower Saxony.

*a.hartmann@uni-oldenburg.de

[1] J. Bricmont and A. Kupiainen, Phys. Rev. Lett. **59**, 1829 (1987).
[2] M. Gofman, J. Adler, A. Aharony, A. B. Harris, and M. Schwartz, Phys. Rev. Lett. **71**, 1569 (1993).
[3] H. Rieger, Phys. Rev. B **52**, 6659 (1995).
[4] U. Nowak, K. D. Usadel, and J. Esser, Phys. A Stat. Theor. Phys. **250**, 1 (1998).
[5] A. K. Hartmann and U. Nowak, Eur. Phys. J. B **7**, 105 (1999).
[6] A. K. Hartmann and A. P. Young, Phys. Rev. B **64**, 214419 (2001).
[7] A. A. Middleton and D. S. Fisher, Phys. Rev. B **65**, 134411 (2002).
[8] C. Frontera and E. Vives, Comput. Phys. Commun. **147**, 455 (2002).
[9] E. T. Seppälä, A. M. Pulkkinen, and M. J. Alava, Phys. Rev. B **66**, 144403 (2002).
[10] A. K. Hartmann, Phys. Rev. B **65**, 174427 (2002).
[11] A. A. Middleton, arXiv:cond-mat/0208182.
[12] M. Zumsande, M. J. Alava, and A. K. Hartmann, J. Stat. Mech. (2008) P02012.
[13] B. Ahrens and A. K. Hartmann, Phys. Rev. B **83**, 014205 (2011).
[14] G. Grinstein, Phys. Rev. Lett. **37**, 944 (1976).
[15] W. L. McMillan, J. Phys. C **17**, 3179 (1984).
[16] A. J. Bray and M. A. Moore, J. Phys. C **17** (1984).
[17] A. K. Hartmann and A. P. Young, Phys. Rev. B **64**, 180404 (2001).
[18] A. K. Hartmann, A. J. Bray, A. C. Carter, M. A. Moore, and A. P. Young, Phys. Rev. B **66**, 224401 (2002).
[19] A. J. Bray and M. A. Moore, in *Heidelberg Colloquium on Glassy Dynamics*, edited by J. L. van Hemmen and I. Morgenstern (Springer, Berlin, 1987), p. 121.
[20] D. S. Fisher and D. A. Huse, Phys. Rev. Lett. **56**, 1601 (1986).
[21] D. S. Fisher and D. A. Huse, Phys. Rev. B **38**, 386 (1988).
[22] A. K. Hartmann and M. A. Moore, Phys. Rev. Lett. **90**, 127201 (2003).
[23] A. K. Hartmann and M. A. Moore, Phys. Rev. B **69**, 104409 (2004).
[24] A. K. Hartmann, Phys. Rev. B **77**, 144418 (2008).
[25] A. K. Hartmann, Phys. Rev. E **59**, 84 (1999).
[26] A. K. Hartmann, Phys. Rev. E **60**, 5135 (1999).
[27] S. Boettcher, Eur. Phys. J. B **38**, 83 (2004).
[28] S. Boettcher and A. K. Hartmann, Phys. Rev. B **72**, 014429 (2005).
[29] S. Boettcher, Phys. Rev. Lett. **95**, 197205 (2005).
[30] M. Zumsande and A. K. Hartmann, Eur. Phys. J. B **72**, 619 (2009).
[31] N. G. Fytas, A. Malakis, and K. Eftaxias, J. Stat. Mech. Theory Exp. (2008) P03015.
[32] R. L. C. Vink, T. Fischer, and K. Binder, Phys. Rev. E **82**, 051134 (2010).
[33] A. J. Bray and M. A. Moore, J. Phys. C **18**, L927 (1985).
[34] J. C. Picard and H. D. Ratliff, Networks **5**, 357 (1975).
[35] A. T. Ogielski, Phys. Rev. Lett. **57**, 1251 (1986).
[36] A. V. Goldberg and R. E. Tarjan, J. Assoc. Comput. Mach. **35**, 921 (1988).
[37] A. K. Hartmann and H. Rieger, *Optimization Algorithms in Physics* (Wiley-VCH, Berlin, 2001).
[38] K. Mehlhorn and S. Näher, *The LEDA Platform of Combinatorial and Geometric Computing* (Cambridge University Press, Cambridge, 1999).
[39] A. A. Middleton, Phys. Rev. Lett. **88**, 017202 (2001).
[40] K. Schwarz, A. Karrenbauer, G. Schehr, and H. Rieger, J. Stat. Mech. Theory Exp. (2009) P08022.
[41] A. K. Hartmann, *A Practical Guide to Computer Simulation* (World Scientific, Singapore, 2009).
[42] S. V. Buldyrev, S. Havlin, E. López, and H. E. Stanley, Phys. Rev. E **70**, 035102 (2004).
[43] O. Melchert, L. Apolo, and A. K. Hartmann, Phys. Rev. E **81**, 051108 (2010).
[44] J.-P. Bouchaud, F. Krzakala, and O. C. Martin, Phys. Rev. B **68**, 224404 (2003).

[45]I. A. Campbell, A. K. Hartmann, and H. G. Katzgraber, Phys. Rev. B **70**, 054429 (2004).
[46]D. S. Fisher, Phys. Rev. Lett. **56**, 416 (1986).
[47]M. Schwartz and A. Soffer, Phys. Rev. Lett. **55**, 2499 (1985).
[48]J. L. Jones and A. P. Young, Phys. Rev. B **71**, 174438 (2005).
[49]V. E. Privman, *Finite Size Scaling and Numerical Simulation of Statistical Systems* (World Scientific, Singapore, 1990).
[50]E. Brézin, J. Phys. (Paris) **43**, 15 (1982).